Probing coherent electronic states in double quantum dots

H. Qin[1], **A. W. Holleitner**[1], **A. K. Hüttel**[1], **R. H. Blick**[*, 1], **W. Wegscheider**[2], **M. Bichler**[3], **K. Eberl**[4], and **J. P. Kotthaus**[1]

[1] Center for NanoScience and Sektion Physik, Ludwig-Maximilians-Universität, Geschwister-Scholl-Platz 1, 80539 München, Germany

[2] Institut für Angewandte und Experimentelle Physik, Universität Regensburg, 93040 Regensburg, Germany

[3] Walter-Schottky-Institut, Technische Universität München, 85747 Garching, Germany

[4] Max-Planck-Institut für Festkörperforschung, Heisenbergstr. 1, 70569 Stuttgart, Germany

Experimental results on both serial and parallel double quantum dots are presented. The quantum dots are realized in the two-dimensional electron gas of an AlGaAs/GaAs heterostructure. By varying the inter-dot tunnel barriers, double quantum dots are tuned from the weak coupling limit to the strong coupling case. In serial double quantum dots, bonding and anti-bonding molecular states are probed by both direct tunneling and photon-assisted tunneling spectroscopy. In parallel double quantum dots, a coherent transport through the whole structure is verified through Aharonov-Bohm oscillations in the magnetotransport data. Furthermore, coherent molecular states are read out by a cotunneling current. Finally, a scheme for preparing and measuring a solid-state quantum bit is discussed.

1 Introduction

With the tools of semiconductor nano-lithography at hand, quantum dots can by now be fabricated in a controlled manner [1–6]. The electron transport through such quantum dots allows one to manipulate and to probe single electrons within a defined interaction volume of a semiconductor host material. The quantum dots provide a perfect tool to exploit the interplay of discrete quantum states with their micro- and macroscopic environment, such as phonons, photons or strain fields. Wave function tailoring and explicit shaping of a particular confinement potential extend the pure analogy between having an artificial atom and a real atom. In addition, the well controlled single electron transistors are precursors for future quantum device applications [7–11]. In order to use the quantum dot states as building blocks for quantum information processing, it is of scientific and engineering interest how to probe the coherent modes within an artificial molecule with minimal perturbation. In this article we review processing and measurements on both serial and parallel double quantum dot devices. We demonstrate how a coherent electron mode, formed in an artificial molecule, can be probed in direct transport measurements as well as in response to an applied microwave signal. In a parallel geometry where the two quantum dots are integrated into the arms of an Aharonov-Bohm interferometer, we show that the transport through the device is partially phase coherent. Utilizing this parallel geometry

---
[*] Corresponding author: e-mail: blick@engr.wisc.edu, Phone: +001 608 262 1952, Fax: +001 608 262 1952. Present address: Department of Electrical Computer Engineering, University of Wisconsin-Madison, 1415 Engineering Drive, Madison WI 53706, USA

for a coupled double quantum dot system, we present a method of how to read out coherent states with minimal perturbation. Finally, possible realizations of charge-based and spin-based quantum bits (qubits) from coupled double quantum dot system are discussed.

2 Single quantum dots

A semiconductor quantum dot is a sub-micron solid-state device containing a small number of free charge carriers (1–1000). Via an electrostatic potential, these charges are confined within lateral dimensions of about the Fermi wave length (∼50 nm). This leads to the formation of discrete binding states (ϵ_i, $i = 1, 2, \ldots$). The quantum state spectrum depends on the shape of the potential well. However, a parabolic confinement usually describes the experimental findings reasonably well [2, 12, 13]. For a quantum dot which is connected to electron reservoirs (the drain and source contacts), the barriers between the quantum dot and the contacts are finite, which results in a continuum of energy states above the discrete binding states.

The electrons in the quantum dot interact both with each other and with the background charges of the crystal lattice. Simplifying the complexity of this many-body system, the constant-interaction model describes the repulsive Coulomb interactions with a constant total capacitance for the quantum dot (C_Σ). To that effect, a charging energy of $E_C = e^2/C_\Sigma$ is required to add an extra electron onto the quantum dot. In the few-electron limit, however, when the orbital and spin structure varies from one electronic state to another, the constant-interaction model needs to be extended towards, e.g., a Hartree-Fock treatment. In this review, we only refer to the constant-interaction model, since it grasps the fundamental transport properties of quantum dots – the Coulomb blockade. For a small enough quantum dot, i.e., a small capacitance, the charging energy can be made sufficiently large such that it exceeds the thermal energy $k_B T$ and the drain-source excitation eV_{ds}. In this case, the electron transport through a quantum dot is blocked. Usually, one manipulates the quantum state via the capacitive influence of a plunger gate or via microwave radiation generated by a nearby antenna. By tuning the voltage applied to the gate, not only the quantum state but also the chemical potential of the quantum dot can be manipulated. In analogy to a transistor, the quantum dot can be tuned from the Coulomb blockaded off state to a read-out state, where the contacts are tunnel coupled to one single electron state within the quantum dot. The tunnel current through this so-called single electron transistor shows oscillations with a periodicity of $\Delta V_g = e/C_g + (\epsilon_N - \epsilon_{N-1})/e\alpha$. C_g is the capacitance between the gate and the quantum dot and $\alpha = C_g/C_\Sigma$ converts a tuning of the gate voltage to a corresponding change of the dot's electrochemical potential. Via the drain-source voltage, one can determine the number of discrete quantum states which are read out simultaneously. If not stated otherwise, this work presents transport spectroscopy of single electronic states, i.e., we present data in the linear transport regime ($eV_{ds} \ll \Delta\epsilon, E_C$). When the tunnel barriers between the dot and the reservoirs are opaque so that $h\Gamma_l \approx h\Gamma_r \ll k_B T$, the life-time broadening is negligible compared to the thermal broadening. The conductance of the single quantum dot can be expressed as [7, 14]

$$g = \frac{e^2}{4k_B T} \frac{\Gamma_l \Gamma_r}{\Gamma_l + \Gamma_r} \cosh^{-2}\left\{\frac{-e\alpha\left[V_g - V_g^\leftrightarrow\right]}{2k_B T}\right\}, \tag{1}$$

where $V_g^\leftrightarrow = (N - 1/2)\, e/C_g + \epsilon_N/e\alpha$ stands for the gate voltage at which the N-th electron can tunnel through the quantum dot, Γ_l and Γ_r are tunneling rates for the left and right tunnel barrier, respectively. For almost transparent tunnel barriers, so that $h\Gamma_l \approx h\Gamma_r \gg k_B T$, the life-time broadening becomes dominant and conductance peaks will have a Lorentzian line shape [7].

3 Experiments

The double quantum dots studied in this review are fabricated within the two-dimensional electron gas (2DEG) of an AlGaAs/GaAs modulation doped heterostructure wafer. Narrow Schottky gates are defined by electron-beam lithography and evaporation of gold on the surface of the wafer. By applying
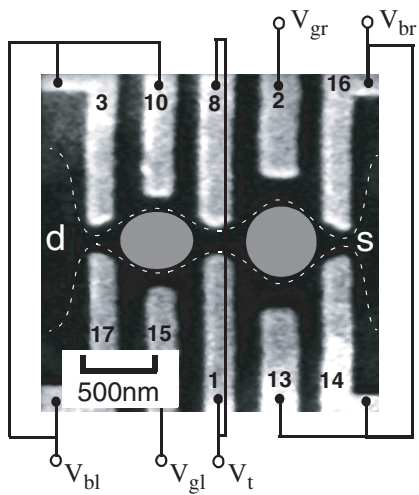
Fig. 1 Scanning electron microscope graph of a double quantum dot formed from the 2DEG of an AlGaAs/GaAs heterostructure (black: substrate surface, white: gold gates). In a typical experiment, the left, right and center tunnel barriers are set by following gate voltages $V_{bl} = -600$ mV, $V_{br} = -670$ mV, and $V_t > -605$ mV. The gate voltages V_{gl} and V_{gr} control the potentials on the left and right dot. The dashed lines roughly mark the boundaries of the 2DEG. The two dots are outlined in two gray areas enclosed by the dashed lines. The device is measured at a bath temperature of $T = 140$ mK.

negative voltages to these gates, the 2DEG beneath the gates are depleted. As shown in Fig. 1, two quantum dots are naturally formed by the geometry of ten gates. The connecting large areas of the 2DEG serve as drain and source contacts, which allow us to drive an electrical current through the double quantum dot. The tunnel barriers between the contacts and the quantum dot are tunable in a wide range, again via the applied gate voltages (e.g., V_{bl} and V_{br} as shown in Fig. 1). The inter-dot coupling can be continuously tuned by gate voltages on appropriate gates (e.g., V_t as shown in Fig. 1).

In our experiments, the quantum dot devices are cooled to a bath temperature of about 40 mK to 900 mK in an Oxford TLM 400 ^{3}He/^{4}He dilution refrigerator. Unless specifically stated, the exact bath temperature at which the experimental data were obtained is recorded in the corresponding figure caption. For measuring the differential conductance, a small sinusoidal signal ($\tilde{v} \sim 10$ μV, $f \approx 17$ Hz) is superimposed on a direct-current (dc) drain-source bias. The resulting alternating current (ac) is amplified by a current amplifier ITHACO 1211 in combination with a low noise EG G 124A analog lock-in amplifier. In the microwave setup, the gigahertz signal is fed through a coaxial cable from an HP83711A synthesizer at room temperature to a Hertzian wire-loop antenna about 1 cm above the device. Both the device and the antenna are thermally anchored at the bath temperatures. The power and frequency of the microwave signal are carefully chosen so that the device is tested in thermal equilibrium. A perpendicular magnetic field can be applied.

4 Serial double quantum dots

In Fig. 1, a double quantum dot is formed by five pairs of Schottky gates on an AlGaAs/GaAs modulation doped heterostructure wafer. The two dots are coupled to each other by a tunnel barrier which is tunable by gate voltage V_t. In order to probe the electronic states in the double dot, the left and right dots are connected to the drain and source electron reservoirs, by tunnel barriers which are controlled by the gate voltages V_{bl} and V_{br}. Furthermore, the electrochemical potentials in the dots can be tuned by the gate voltages V_{gl} and V_{gr}.

In Fig. 2, the double quantum dot is modeled as a network of tunnel resistors and capacitors. The two quantum dots and the drain and source contacts are connected in series by three tunnel junctions. The coupling of the quantum dots to the reservoirs and the inter-dot tunnel coupling can be quantified by following tunneling rates: Γ_l, Γ_r and Γ_t, as shown in Fig. 2. Gate voltages V_{gl} and V_{gr} are coupled to the left and right quantum dot through the gate capacitors C_{gl} and C_{gr}, respectively. Each gate voltage is also cross coupled to the other quantum dot through the capacitors C_{rl} or C_{lr}, as shown in Fig. 2. The charging energy for each quantum dot can be expressed as $E_{Cl/r} = e^2/C_{\Sigma l/r}$, where $C_{\Sigma l}$ and $C_{\Sigma r}$ are the total capacitance for the left and right dot.
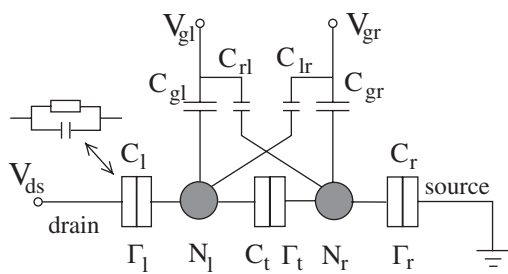
Fig. 2 Equivalent circuit for a coupled double quantum dot as shown in Fig. 1. The tunnel barriers are described by a tunnel resistance shunted with a junction capacitance.

4.1 Electrostatic coupling regime

In a double quantum dot device, electrostatic charging is always present between the two quantum dots. In order to probe charge transport through a double dot, it is necessary to couple the two dots via a tunnel barrier. However, the inter-dot tunneling can be neglected when it only serves as a perturbation to the system energy. In this electrostatic coupling regime, the inter-dot tunneling only slightly perturbs the electron numbers of the two dots. We can define chemical potentials for the double quantum dot as following

$$\mu_l(N_l, N_r - 1) = E(N_l, N_r - 1) - E(N_l - 1, N_r - 1) , \tag{2}$$

$$\mu_r(N_l - 1, N_r) = E(N_l - 1, N_r) - E(N_l - 1, N_r - 1) , \tag{3}$$

$$\mu_{lr}(N_l, N_r) = \mu_l(N_l, N_r - 1) - \mu_r(N_l - 1, N_r) = E(N_l, N_r - 1) - E(N_l - 1, N_r) , \tag{4}$$

where, $E(N_l - 1, N_r - 1)$ is the ground-state energy of the system with $N_l - 1$ electrons in the left quantum dot and $N_r - 1$ electrons in the other. The discrete binding states of both dots are included in $E(N_l - 1, N_r - 1)$. The chemical potential $\mu_l(N_l, N_r - 1)$ (if $= \mu_d$) represents the ground state at which the system allows an electron to tunnel between the drain and the left dot while the number of electrons on the the right dot is kept constant: $(N_l - 1, N_r - 1) \leftrightarrow (N_l, N_r - 1)$. Similarly, the chemical potential $\mu_r(N_l - 1, N_r)$ (if $= \mu_s$) represents the ground state at which the system allows an electron to tunnel between the source and the right quantum dot: $(N_l - 1, N_r - 1) \leftrightarrow (N_l - 1, N_r)$. The chemical potential $\mu_{lr}(N_l, N_r)$ (if $= 0$) refers to the ground state level at which the system allows an electron to tunnel between the two quantum dots: $(N_l, N_r - 1) \leftrightarrow (N_l - 1, N_r)$. As stated above, $\mu_{l/r}$ represents the chemical potential for the whole system at which an electron in the drain/source contact can occupy or evacuate the lowest available single electron state in the left/right dot. For simplicity, we directly refer μ_l and μ_r to the single electron states ϵ_l and ϵ_r in the left and right quantum dot, respectively.

By sweeping the gate voltages V_{gl} or V_{gr}, both quantum dots can be tuned independently from a Coulomb blockade state to a read-out state where a drain-source current probes the system. Following Eqs. (2, 3, and 4), the allowed tunnel conditions yield a honeycomb pattern in a $V_{gr} - V_{gl}$ plane which is called the charging diagram of the double quantum dot [5, 15–19] (see Fig. 3). In the diagram, the boundaries B1 and B2 are determined by Eqs. (2) and (3), respectively. Along these boundaries, a single electron can occupy the lowest unoccupied single electron quantum state in one of the dots, while the single electron state in the other dot is not accessible (as schematically shown in Fig. 3 (b, d)). Only when both conditions are satisfied so that both single electron states become accessible (as shown in Fig. 3 (c)), i.e., at the crossing point p1, single electrons can tunnel through the system. At crossing point p1, the double dot can only accept one extra electron, but both dots are able to accept this extra electron. The nearby crossing point p2 stems from another set of B1 and B2 transitions with one more electron on each dot. On the line between p1 and p2, one extra electron is added to the double dot. Since the chemical potentials of both dots are equal, i.e., $\mu_l = \mu_r$, this electron can stay on one or the other dot. Electron transport in this region is normally blocked because $\mu_l = \mu_d$ and $\mu_r = \mu_s$ are not met at the same time. Moving from point p1 to p2, each quantum dot obtains an extra electron. The voltage difference, in order to move from p1 to p2, is determined by the inter-dot
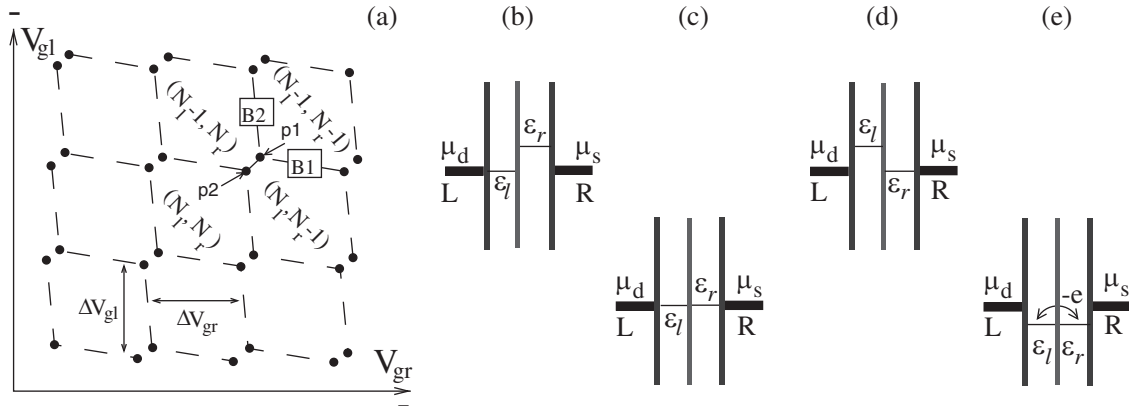
Fig. 3 (a) Charging diagram: the direct current/conductance as a function of the left and right gate voltages yields a honeycomb pattern. In the diagram, finite current/conductance is represented by black dots. Boundaries B1 and B2 intersect at the crossing point p1. The schematic ground-state configurations along boundary B1, at crossing point p1, along boundary B2, and along line p1–p2 are shown in (b), (c), (d), and (e), respectively.

Coulomb charging energy $E_{el} = 2e^2 C_t/(C_{\Sigma l} C_{\Sigma r})$, which is proportional to the inter-dot capacitance C_t [16, 17, 19].

In linear transport regime ($eV_{ds} \ll E_{el} < E_{Cl/r}$), the single electron states can only be read out when $\mu_{d/s} \leq \mu_l = \mu_r \leq \mu_{s/d}$, i.e., at crossing points. The period by which the appearance of crossing points alternate in gate voltages V_{gl} and V_{gr}, are determined by the charging energy of each quantum dot [20]: $\Delta V_{gl/r} = e/(\gamma_{gl/gr} C_{\Sigma l/r}) = e/\tilde{C}_{gl/gr}$, where γ_{gl} and γ_{gr} are coefficients determined by the dot/gate capacitances. $\tilde{C}_{gl}$ and $\tilde{C}_{gr}$ are effective gate capacitances. They differ slightly from C_{gl} and C_{gr} due to the non-zero cross capacitances C_{rl} and C_{lr} [16, 19].

Experimentally, the ground states are probed in the linear transport regime while both gate voltages are swept. Figure 4 (a) shows a charging diagram of the double dot device shown in Fig. 1 in grayscale. Since the tunnel coupling is weak, the tunnel current is strongly suppressed along the hexagon boundaries (solid lines). Strong tunneling is observed around crossing points (white circles). From
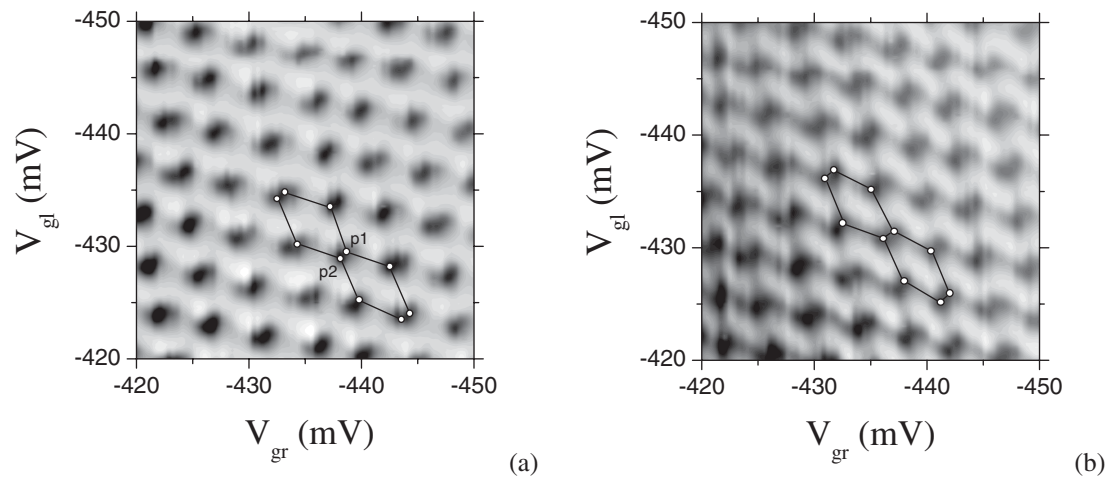

Fig. 4 Charging diagrams from dc measurement of (a) the weakly coupled and (b) the strongly coupled double dot are shown in the linear grayscale representation. In (a), white: $I_{ds} \approx -1.5$ pA, black: $I_{ds} \leq 12$ pA. In (b), white: $I_{ds} \approx -1.5$ pA, black: $I_{ds} \leq 18$ pA. Accordingly, the central gate voltage V_t is −590 mV and −580 mV. In both cases, the drain-source bias is less than +50 µV and $T = 140$ mK.

photon-assisted tunneling (see Sec. 4.3) and nonlinear transport measurements, equivalent-circuit parameters as shown in Fig. 2 can be obtained. The total capacitance for the left and right dot are $C_{\Sigma l} \approx 6.93 \times 10^{-16}$ F and $C_{\Sigma r} \approx 7.55 \times 10^{-16}$ F, corresponding to the charging energy of 231 µeV and 212 µeV, respectively. The mean level spacing in both dots is about $\delta\epsilon^* \approx 120$ µeV. The inter-dot Coulomb charging energy is found to be $E_{el} \approx 50$ µeV for the weak coupling case shown in Fig. 4 (a) and $E_{el} \approx 91$ µeV for the case in Fig. 4 (b). The dot-contact tunneling rates ($\Gamma_{l/r}$) are verified to be about 100 MHz ($h\Gamma_{l/r} \ll k_{\rm B}T$). At a finite temperature ($k_{\rm B}T \sim E_{el}$), however, the energetic selection rules are overcome by thermally activated electrons. Then, the tunnel current is also detectable in the vicinity of points p1 and p2 and the two points seem to 'have merged together'. In a stronger coupling regime (see Fig. 4 (b)), the tunnel current also appears at the boundaries of the honeycomb pattern and the separation of p1 and p2 becomes larger. This regime will be described in the next section.

4.2   Tunnel coupling regime

When the inter-dot tunnel coupling is strong enough, an electron can tunnel back and forth between the two quantum dots coherently. The electronic wave function expands throughout both quantum dots so that this electron is shared by either quantum dot. We only consider the case in which one single electron is delocalized across the double dot, which corresponds to the bonding state of the artificial molecule. The case of two delocalized electrons would require an even stronger tunnel coupling: $2t \approx 2h\Gamma_t > E_{Cl/r} - E_{el}$.

Given an electron can tunnel back and forth between the dots coherently [21–23] and the double dot is singly occupied, the ground state of the double quantum dot system is then a superposition of ground state $|N_l - 1, N_r\rangle$ and $|N_l, N_r - 1\rangle$:

$$|N\rangle = a|N_l - 1, N_r\rangle + b|N_l, N_r - 1\rangle , \tag{5}$$

which forms a bonding molecular state. The corresponding anti-bonding state occurs as the lowest excited state. The coefficients in Eq. (5) depend on the detuning of the two ground states of the decoupled system ($\delta E = \epsilon_l - \epsilon_r$) and the tunnel coupling ($t \approx h\Gamma_t$). The corresponding energies for the bonding and anti-bonding states are

$$E_- = \bar{\mu} - \tfrac{1}{2}\left\{ \sqrt{(\delta E)^2 + 4t^2} \right\} , \tag{6}$$

$$E_+ = \bar{\mu} + \tfrac{1}{2}\left\{ \sqrt{(\delta E)^2 + 4t^2} \right\} , \tag{7}$$

where, $\bar{\mu} = (\epsilon_l + \epsilon_r)/2$. The gap between the molecular states is

$$E_+ - E_- = \sqrt{(\delta E)^2 + 4t^2} , \tag{8}$$

which can be tuned by the gate voltages V_{gl} and V_{gr}.

In Fig. 5 (a) and (b), the molecular states are illustrated in a level diagram and plotted as a function of the detuning. Due to the coherent coupling, an electron which is initially occupying one of the dots will start to oscillate between the two dots at a frequency of $\Omega = (E_+ - E_-)/h$ [21, 23]. This coherent charge oscillation decays according to a dephasing rate $1/\tau_{\rm coh}$:

$$\rho(t) = \frac{4t^2}{\hbar^2 \Omega^2} \, e^{-t/\tau_{\rm coh}} \sin^2\left(\frac{\Omega t}{2}\right) . \tag{9}$$

The coherent oscillation is most prominent when the detuning diminishes to zero ($\Omega \to \Omega_0 = 2t/h$). With increasing detuning, the oscillation fades out on a faster timescale, and the double quantum dot is best described by the localized quantum dot states again. The oscillation is triggered whenever an electron tunnels from the leads onto the quantum dot, and it is terminated when the electron tunnels back to one of
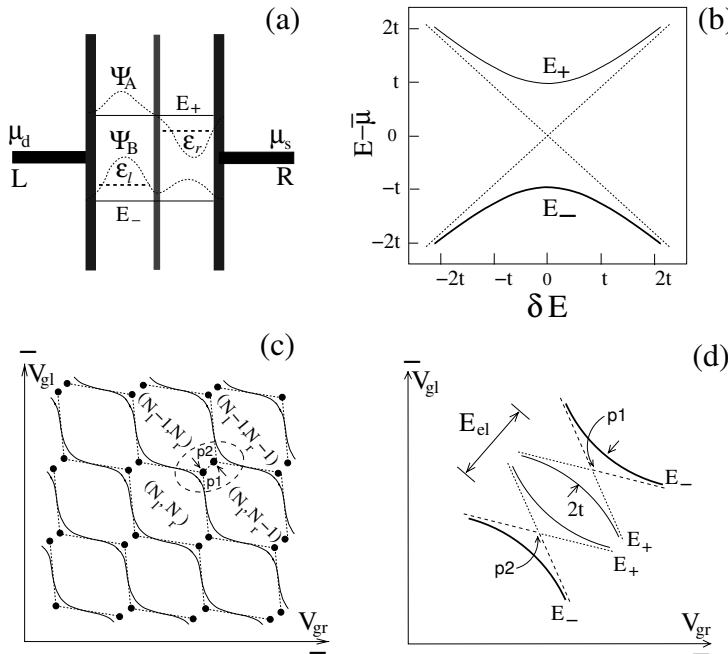
Fig. 5 (a) A level diagram illustrates the formation of a bonding (E_-) and an anti-bonding (E_+) molecular state in a double dot. The dashed lines represent the ground states of the decoupled quantum dots (ϵ_l and ϵ_r). (b) The bonding and the anti-bonding molecular state as a function of the detuning ($\delta E = \epsilon_l - \epsilon_r$). (c) Charging diagram of a tunnel coupled double quantum dot. (d) Under a finite drain-source bias, transport through the bonding and anti-bonding molecular states can be observed in the vicinity of each crossing point. Tunneling through the bonding state is shown on the corresponding thick solid line, while tunneling through the anti-bonding state is on the thinner solid line. The double dot is assumed to be singly occupied even on the solid line beyond the crossing point p2.

the leads. This occurs at a rate of $\bar{\Gamma} = (\Gamma_l + \Gamma_r)/2$. The contribution of this process to the dephasing of the coherent state can be minimized by decoupling or isolating the molecular states from the contacts.

The existence of molecular states changes the charging diagram drastically, as depicted in Fig. 5 (c). The tunnel current through bonding molecular states can be detected along the honeycomb boundaries (solid lines in Fig. 5 (c)). Tunneling through the anti-bonding molecular states occurs in the region between each paired crossing points (p1 and p2). Figure 5 (d) is a close-up showing the additional features from anti-bonding molecular states probed by a finite drain-source bias.

An experimental charging diagram for a strongly coupled double quantum dot is shown in Fig. 4 (b). The transport, which arises from charge fluctuations between the two dots, can now be seen along the honeycomb boundaries and is maximized around the crossing points. Both can be explained by the fact that the electrons are delocalized although the two quantum dot energy levels are not degenerate (for comparison Fig. 4 (a) depicts the weak coupling regime). Figure 6 (a) shows a charging diagram in an even stronger tunnel coupling regime. The crossing points p1 and p2 are separated even further from each other. A single trace taken from the charging diagram around the crossing points p1 and p2 is displayed in Fig. 6 (b). By fitting the curves to Eq. (1), the bonding and anti-bonding states are resolved.

4.3 Photon-assisted tunneling

Quantum states in a semiconductor quantum dot are always exposed to various fluctuations of the environment, such as the very high frequency electromagnetic fields from black body radiation, both acoustic and optical phonons from the semiconductor host materials, and low frequency random tele-
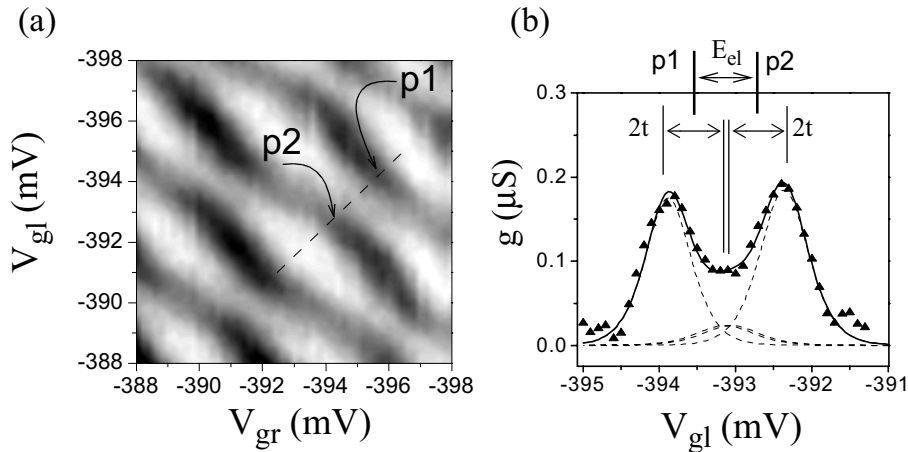
Fig. 6 (a) The charging diagram from the conductance of the strongly coupled double quantum dot ($V_t = -560$ mV, white: $g \approx 0$ μS, black: $g < 0.5$ μS). (b) A single trace is extracted along the dashed line shown in (a). The fit of this curve distinguishes the tunnel current through the bonding and anti-bonding molecular states. $T = 140$ mK.

graph switching from background charges. All these can induce inelastic relaxations of the quantum states, which is usually referred to as dephasing. The idea to control quantum states and to define concrete quantum device applications motivates studies on dephasing and the dynamics of coherent states. Photon-assisted tunneling through single quantum dots has been intensively studied [6, 24–27] and provides a powerful tool for exploring the interaction between an artificial atom and an electromagnetic field [28–31]. The transition frequency for typical quantum dot states lies in the microwave range of a few GHz (10^9 Hz).

In the absence of microwave excitation, as stated in Section 4.2, a single electron is mainly localized in one of the dots when $\delta E \neq 0$, e.g., in the left dot as shown in Fig. 7 (a) or in the right dot as shown in Fig. 7 (b). When only a small V_{ds} is applied and the bonding state is located below the transport window, electron transport is not allowed. With microwave radiation, however, transitions between the molecular states with $\delta E \neq 0$ can be realized if the photon energy is in resonance with the molecular states [21, 22]:

$$hf = E_+ - E_- = \sqrt{(\delta E)^2 + 4t^2}\,. \tag{10}$$
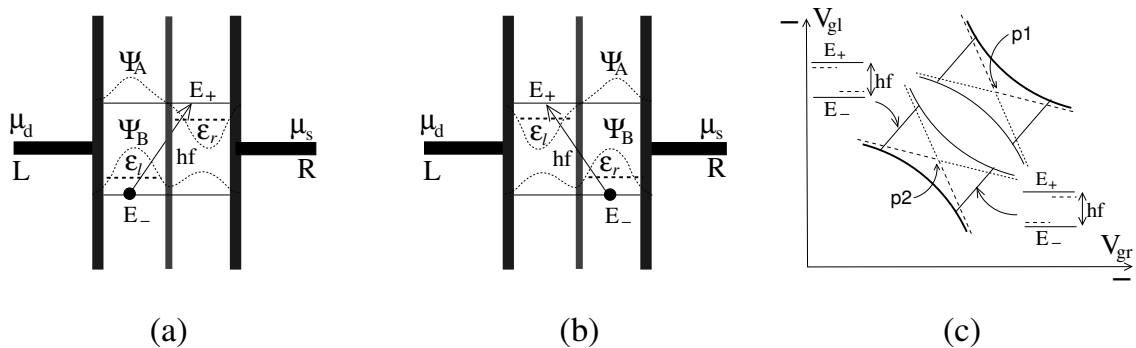

Fig. 7 In the linear transport regime, large energy detuning between the left and right quantum states localize the electron in the left dot or in the right dot, as shown in level diagram (a) and (b), respectively. Microwave photons can couple the bonding and anti-bonding molecular states. (c) Under microwave radiation, photon side-peaks appear on either side of the crossing points.
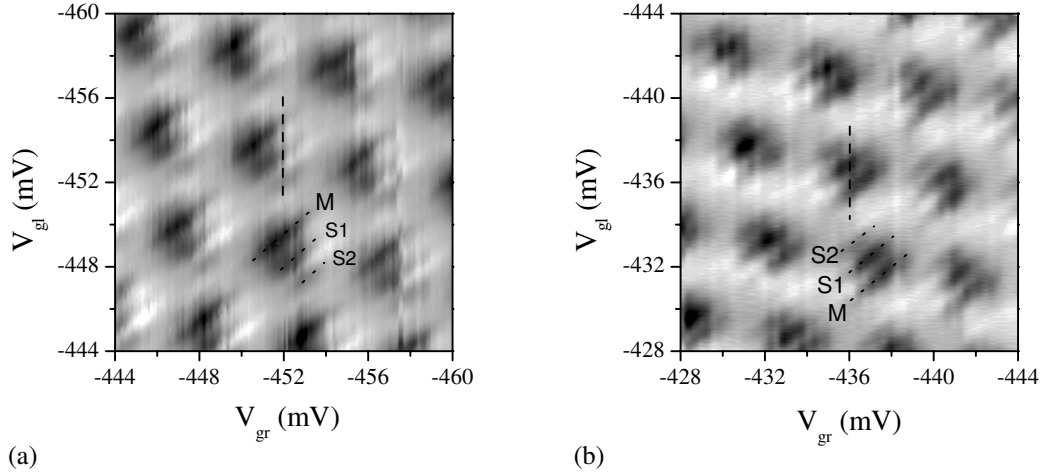
Fig. 8 Under microwave radiation of $f = 20$ GHz, the charging diagrams (direct current) are measured with a small (a) negative ($V_{ds} = -30$ μeV, white: $I_{ds} > -0.6$ pA, black: $I_{ds} < 1.3$ pA) and (b) positive ($V_{ds} = +30$ μeV, white: $I_{ds} < -0.5$ pA, black: $I_{ds} < -1.9$ pA) drain-source bias. The one-photon sidepeak (S1) and the two-photon sidepeak (S2) are located beside the main peak (M). $T = 140$ mK.

A forward or reverse tunnel current is induced by this coherent pumping, as schematically shown in Fig. 7 (a, b). As shown in the charging diagram in Fig. 7 (c), additional photon side bands in tunnel current appear on both sides of the crossing points p1 and p2. Given a large bias is applied ($eV_{ds} > E_{+} - E_{-}$), electrons can also emit photons and the reverse pumping current will be suppressed.

The state of a double dot at n-photon resonance condition is a coherent superposition of the two-level system by n photons [21, 22]. This can be understood in terms of the hybridization of wavefunction on one dot with the wave function of the n-th photon sideband on the other dot. For example, when the n-th photon sideband of quantum state ϵ_l of the left dot matches the quantum state ϵ_r of the right dot, the inter-dot tunneling will hybridize the two states. The effective coupling between the
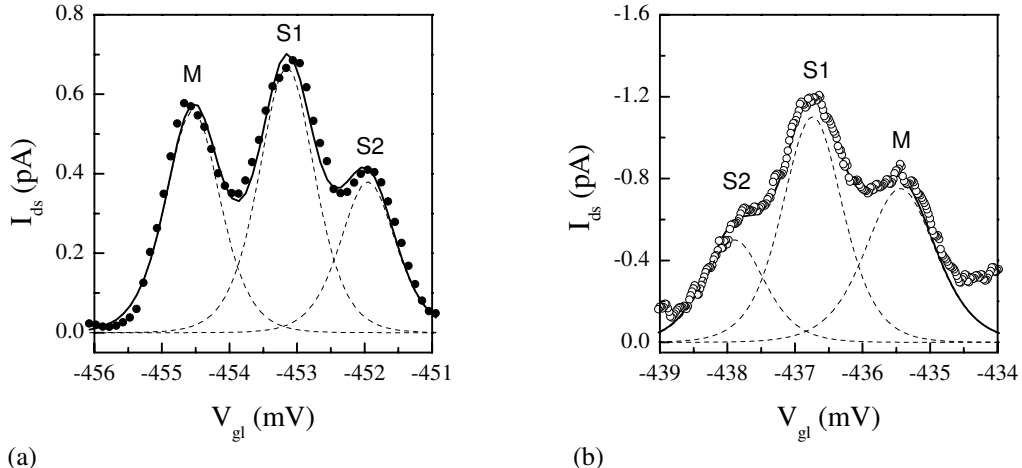

Fig. 9 Single traces (a) and (b) are extracted from the charging diagrams at constant V_{gr} marked by the dashed lines as shown in Fig. 8 (a) and (b), respectively. The solid curve is a fit with three $\cosh^{-2}((\delta E - nhf)/wk_B T)$-shaped peaks with $w \approx 2.3$ (as shown by the dashed curves), where $n = 0, 1, 2$ corresponds to M, S1 and S2, respectively.
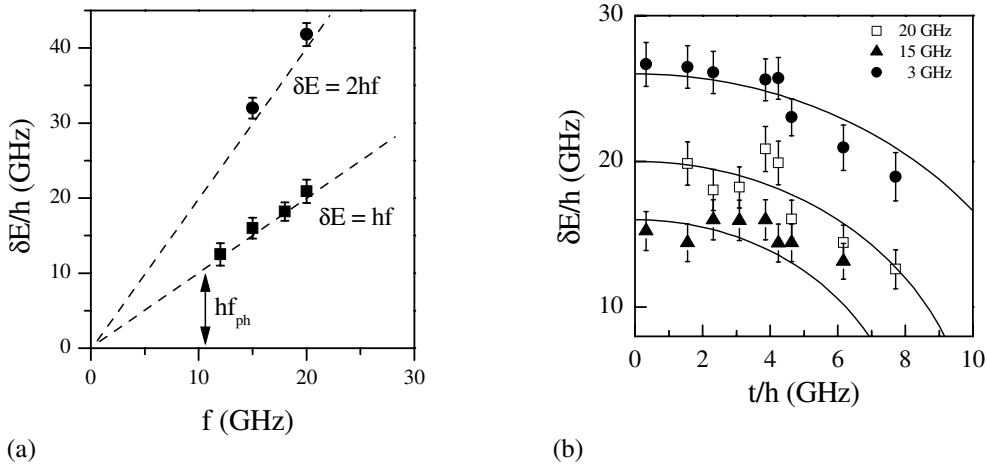
Fig. 10 (a) The detuning of photon sidepeaks at different frequencies in the weak coupling regime. (b) The detuning of photon sidepeaks at different frequencies with varying the coupling strength. The solid curves for $f = 15$ GHz and $f = 20$ GHz are fits based on Eq. (10). The solid curve for $f = 3$ GHz is a fit from Eq. (11) with $f_{\mathrm{ph}} = 10$ GHz.

wavefunctions becomes the product of t and the amplitude of the sideband $J_n(e\tilde{V}/hf)$, where $J_n(x)$ is the Bessel function of the first kind, and $\tilde{V}$ is the amplitude of the electric-field component in the radiation. A single electron is then delocalized between the quasi-eigenstates, oscillating at a Rabi frequency of $\Omega = 2tJ_n(e\tilde{V}/hf)/h \leq \Omega_0$.

In Fig. 8 (a) and (b), photon-assisted tunneling under microwave radiation of 20 GHz is shown in charging diagrams obtained at a negative and positive drain-source bias, respectively. The bias amplitude applied is set to 30 μeV (corresponds to about 7.2 GHz) so that it is high enough to suppress the reverse pumping current. A higher bias would induce extra broadening in the resonances. Beside the main peak (at which $\delta E = 0$), photon sidebands, which correspond to one-photon and two-photon resonances, are observed, as indicated with S1 and S2 in Fig. 8. The reversed pumping current is suppressed by a forward current and the corresponding sideband is less visible. In Fig. 9, single curves taken from Fig. 8 show clearly the main peak and two sidepeaks.

In Fig. 10 (a), the detuning (δE) at the sidepeaks is plotted versus microwave frequency. The detuning for one-photon (S1) and two-photon (S2) absorption process is approximated by the relevant photon energy: $\delta E_1 = hf$ and $\delta E_2 = 2 \times hf$. This dependence is expected for a weakly coupled double quantum dot (see Eq. (10) with $t \ll \delta E$). The existence and control of molecular states are further examined by measuring charging diagrams at different tunnel coupling. The coupling dependence of the detuning of two quantum states at the photon sidepeaks is shown in Fig. 10 (b). We find that at $f = 15$ GHz and $f = 20$ GHz the detuning at sidepeak S1 follows Eq. (10).

Commonly, one expects no coherent superposition of the molecular states below $f = 8$ GHz since the thermal fluctuation ($k_{\mathrm{B}}T/h \approx 3.5$ GHz) becomes comparable to the photon energy and an effective coupling of the double dot to a phonon mode around 10 GHz is observed (for details see Ref. [32] and Ref. [33]). However, we observe coherent superposition of molecular states below 8 GHz [32]. At 3 GHz as shown in Fig. 10 (b), we observe a strong sidepeak from a coherent two-photon and two-phonon resonance:

$$\delta E_2 = \sqrt{(2hf + 2hf_{\mathrm{ph}})^2 - 4t^2}\,, \tag{11}$$

with $f_{\mathrm{ph}} = 10$ GHz. The reason is that Schottky gates on the heterostructure surface not only define the quantum dots, but also form phonon cavities since the sound velocity of surface acoustic waves decreases under the metalized regions. Most importantly, the applied microwave field enhances via

piezoelectric coupling the interaction between confined electrons and cavity phonon modes. Assuming a sound velocity of 2800 m/s for surface acoustic waves or 4500 m/s for bulk phonons in the GaAs crystal, the observed 10 GHz phonon mode yields a wavelength of 280 nm or 450 nm, which roughly agrees with the dot's diameter as shown in Fig. 1. This piezoelectric resonator formed by limited number of gates has a large bandwidth in comparison to conventional interdigital transducers. It is the coherent phonons generated by microwave radiation that ensures a coherent superposition of molecular states [32].

In summary for this section, we connect two quantum dots of medium size and probe the coherent superpositions of two molecular states under near-zero bias by using photon-assisted tunneling. The applied microwave radiation introduces coherent microwave photons and acoustic phonons. Apart from conventional photon-assisted tunneling, we find a coherent superposition of photon- and phonon-assisted tunneling, which stems from the superposition of molecular states by both microwave photon and acoustic phonon excitation.

5   Parallel double quantum dot

Cryogenic transport spectroscopy allows us to probe electronic states of single and coupled quantum dots. Due to the thermal excitation ($k_\text{B}T$) and the finite tunnel coupling of quantum states to the contacts ($h\Gamma_{l/r}$), dephasing of the coherent quantum states is ubiquitous. In the Coulomb blockade regime, where $E_C > \mu_d - \mu_s$ and the quantum State stays below μ_d and μ_s, first order tunneling is suppressed. However, higher order tunnel processes allow an electron to tunnel through the dot via virtual states [34]: an electron tunnels from a virtual state in the dot to one of the contacts, while simultaneously another electron tunnels from the contacts onto the same or a different virtual state in the quantum dot. When only one virtual state is involved, this process is called elastic cotunneling. If two virtual states are involved, it is termed inelastic cotunneling. Generally speaking, the cotunneling is enhanced when the dot-contact coupling becomes stronger.

In a serial double quantum dot, the cotunneling contribution of the transport between the dots is observed along the honeycomb boundaries in the charging diagrams, where the two quantum states are largely detuned. Cotunneling through the whole double dot is expected to occur when the two dots are in the Coulomb blockade configuration. However, this effect is very weak unless the two dots are strongly coupled to the contacts.

In a parallel double quantum dot configuration, as schematically shown in Fig. 11, each contact is connected to both quantum dots by two tunnel barriers. An electron in the source contact can tunnel via both quantum dots to the drain contact. This configuration forms an Aharonov-Bohm (AB) ring structure, in which an AB-phase can be accumulated by an electron tunneling through the double dot. This allows us to detect AB oscillations in order to examine the phase coherent transport through the quantum dots. At the same time, the gate geometry in Fig. 11 (b) opens the possibility to tunnel couple both dots and to probe molecular states in the double quantum dot. Since two quantum dots are connected in parallel, the cotunneling contribution of the current becomes strong enough for probing the coherent states which are tuned to below the chemical potentials in the contacts. This implies that quantum bits (qubits) [35] can be prepared without severe dephasing from the contacts. Probing entanglement and nonlocality of electron spins in such a parallel double quantum dot has been proposed and theoretically studied by Loss and Sukhorukov [36]. Experimentally, we have confirmed the coherent transport through such a parallel double quantum dot and observed coherent coupling between the dots [37, 38].

In order to realize an AB ring geometry with the drain/source contact coupled to both quantum dots, the contact regions are covered by a 45 nm thick layer of negative electron-beam resist (calixarene). *Gate* 1 and *Gate* 2 are deposited directly on the substrate surface only in the area where the inter-dot tunnel barrier is to be defined. Other parts of *Gate* 1 and *Gate* 2 are supported by the calixarene acting as insulating spacer. Quantum dot 1 and dot 2 are finally confined by the other six gates which are grouped into the left and right gate, respectively (see Fig. 11). The gate left and right are
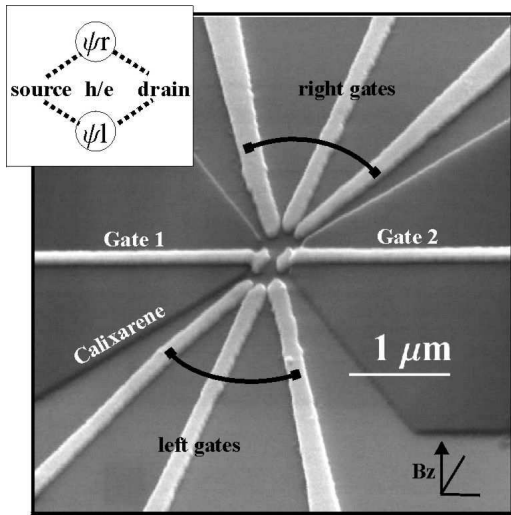
Fig. 11 A scanning electron microscope graph of a parallel double dot. The inset shows the schematic view of the center part. Two quantum dots are connected in parallel to source and drain contacts. The tunneling paths of both electron partial waves define an Aharonov-Bohm interferometer which senses magnetic flux quanta of h/e of an applied field B_z. The 'right' and 'left' gates control the two dot states ψ_r and ψ_l. Essential for the parallel electronic access, *Gate* 1 and *Gate* 2 are patterned on an additional dielectric layer, which is formed by the e-beam resist calixarene.

also used to tune the dot potentials. The AlGaAs/GaAs heterostructure is the same as that for serial double dots studied in the previous section. In Ref. [39], detailed fabrication processes are provided.

5.1 Weak coupling regime

When the two parallel dots are weakly coupled, the inter-dot tunneling and hence the corresponding charge transport can be neglected. The total current reflects the sum of the partial currents through each individual dot which can be seen in the pseudo 3D presentation of the top panel of Fig. 12. In this weak coupling regime, the charging diagram resembles similar honeycomb patterns as shown in Fig. 3 (a) for a serial double dot. However, a current can be measured along all honeycomb boundaries (given an intermediate dot-contact coupling $h\Gamma \sim \delta\epsilon^*$). A small gap between the crossing point p1 and p2 is also expected, although this can be diminished when the thermal energy becomes comparable to the inter-dot charging energy, as has been shown in Fig. 4. If the phase coherence is preserved in the transport through the double dot, the tunnel current develops AB oscillations every time when the magnetic flux through the ring area is changed by h/e. In Fig. 12 (a), a charging diagram shows the area around a crossing point where two resonant tunnel current bands intersect [37, 39, 40]. AB oscillations are examined at resonant and off-resonant conditions as shown in Fig. 12 (b), where clearly AB oscillations with a period of 16.8 mT are observed at resonant condition but not in the off-resonant case. According to the area ($\approx 2.5 \times 10^{-13}$ m²) enclosed by the ring, this oscillation period
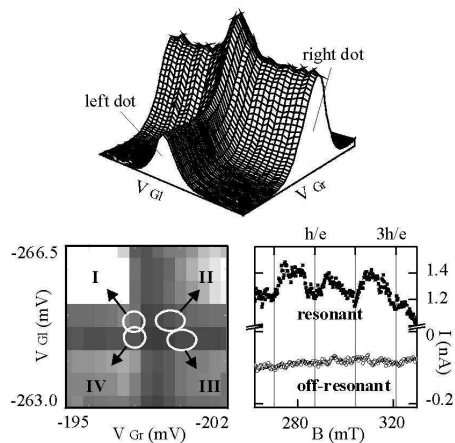

Fig. 12 The bottom-left graph is a charging diagram showing a crossing point, at which the tunnel current is a sum of those two individual tunnel currents through the two dots, as shown in the top graph. The bottom-right graph shows AB oscillations of tunnel current at resonance and off-resonant (bath temperature of $T = 100$ mK and $V_{SD} = 67$ μV).
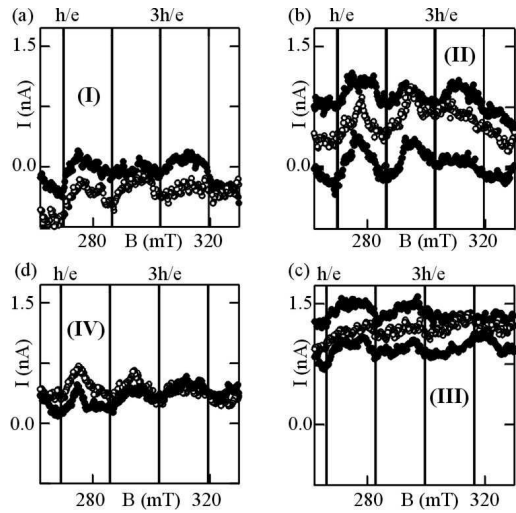
Fig. 13 Phased-locked AB oscillations are observed at locations I, II, III, and IV in the charging diagram shown in Fig. 12. The AB-amplitudes do not show a specific dependence on the number of electrons on the two quantum dots.

agrees with the flux quantum $\Phi_0 = h/e$. AB oscillations are examined in more details around the crossing point shown in Fig. 12 (a). AB oscillations at sites I, II, III, and IV are shown in Fig. 13 (a), (b), (c), and (d), respectively. All show at least four periods of oscillations. Since the measurements are taken in a two-terminal configuration, the AB phase is supposed to be locked [41, 42], which is confirmed in Fig. 13. Generally, AB oscillations imply that at least part of the charge transport through the dots is coherent. The circumference of the ring area which encloses both arms gives a lower limit for the coherence length ($l_\phi \geq 1.8\,\mu\text{m}$) for electrons traversing the dots in this device. From the electron state lifetime (Γ^{-1}) in the dots, we estimated a lower limit for the coherence time to be $\tau_{\text{coh}} \geq 2$ ns [40]. We would like to mention that AB oscillations have also been detected in an AB ring with only one quantum dot embedded [43, 44]. With a parallel double dot structure, however, we are able to not only examine the overall phase coherent transport but also probe the local coherent coupling between the dots and its effect on coherent transport.

5.2 Strong coupling regime

When the inter-dot tunnel coupling becomes stronger, inter-dot charge fluctuation modifies the ground state energy of the double dot. The first effect from this stronger coupling is that the crossing points p1 and p2 are positioned further away from each other than in the weak coupling case. The charging diagram resembles to that shown in Fig. 4 (b) [37]. Here, we only consider the case where both dots are weakly coupled to the contacts. As a result, Coulomb blockade oscillations contributed from single dots will be largely suppressed, which corresponds to a weak tunnel current along the honeycomb boundaries. With a near-zero drain-source bias, we observed strong conductance lines in parallel to the line connecting p1 and p2 (see Fig. 14 (a)) [38].

According to the first order tunneling, transport through the double dot is not allowed between the crossing points p1 and p2. The observed strong transport at crossing points is about two orders of magnitude larger than the normal resonant tunneling through one of the dots (Fig. 14). We attribute this enhanced transport to cotunneling which allows two electrons simultaneously to tunnel through virtual states of the double quantum dot. Mainly due to the presence of strong cotunneling, no discrete molecular states are probed between crossing point p1 and p2, as compared to the serial double quantum dot of Fig. 5 and Fig. 6. However, nearby p1 and p2, in the direction perpendicular to line p1–p2, well resolved Lorentzian shaped tunnel peaks are observed (see Fig. 14) [38]. Different peaks correspond to different detuning between two decoupled quantum states, and hence different degenerate molecular states. By reducing the inter-dot tunnel barrier, more molecular states are observed. The importance of this observation lies in the fact that molecular states which are decoupled from contacts
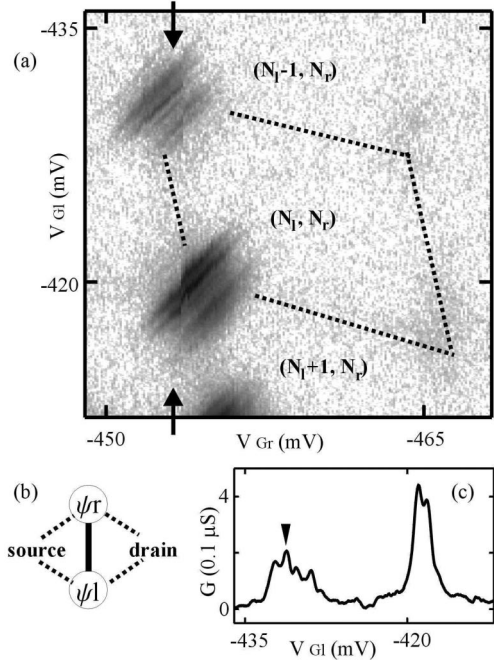
Fig. 14 (a) At a bath temperature of $T = 815$ mK, the parallel quantum dot device is tuned into a regime where only cotunneling via molecular states contributes to the drain-source current. The dashed lines mark positions in the charging diagram where sequential tunneling is prevented because of highly opaque tunnel barriers. Independent of the number of electrons on the double quantum dot (N_l, N_r), a finite conductance due to cotunneling occurs when two coupled dot states ψ_r and ψ_l are connected to source and drain in parallel (see (b)). The single line graph in (c) highlights a set of cotunneling peaks (e.g., black triangle) and refers to the section between the two arrows in (a).

can be non-invasively probed by a cotunneling current. The analysis of the line shape reveals that the broadening (≤ 70 µeV) of cotunneling contribution to the current is only about half of the broadening (≈ 130 µeV) of a normal resonant tunnel peak, which surprises since the thermal broadening is about $3.52 k_B T \approx 247$ µeV for $T \approx 815$ mK. In a detailed theoretical analysis (see [45]), we found that the broadening of the cotunneling resonances reflects mainly the line width of the molecular states themselves in combination with a pseudo-spin Kondo effect. Generally speaking, the spin Kondo effect describes electron correlations between quantum states in the contacts and degenerate spin states in a quantum dot or a spin impurity [46−51]. In a parallel double quantum dot, however, the two electron states with one electron being in either of the two quantum dots are degenerate in charge, even without considering their spin quantum number. The orbital structure of the wave functions acquires spin like features, which can be expressed in terms of a so-called pseudo-spin [52−55]. The pseudo-spin Kondo correlations give rise to second order tunneling, which was experimentally verified in the presented parallel double quantum dot geometry [45].

6   Double quantum dot qubits

As shown in Sec. 4.2, molecular states formed in a strongly coupled double quantum dot can be viewed as a coherent superposition of the decoupled localized states

$$|\phi\rangle = \alpha|l\rangle + \beta|r\rangle , \tag{12}$$

where $|l\rangle = |1, 0\rangle$ and $|r\rangle = |0, 1\rangle$ correspond to the topmost electron occupying the left and right dot, respectively. With $|l\rangle \equiv |0\rangle$ and $|r\rangle \equiv |1\rangle$ as calculation basis, such an artificial molecule provides a versatile candidate for the definition of a qubit, the information register of the proposed quantum computer. To prepare the qubit from a double quantum dot in a defined state, one can set a large detuning between the two base states ($\epsilon_l \ll \epsilon_r$), achieving relaxation into an initial state $|0\rangle = |l\rangle$. In a following step, e.g., a dc pulse signal can be applied to the left gate voltage to meet the condition $\epsilon_l = \epsilon_r$ such that a superposition and via the tunneling a one-qubit rotation is achieved. By the pulse, a wide range of qubit states $|\phi\rangle$ as shown in Eq. (12) can be formed, where α and β are determined by the pulse duration.

An alternative, but equivalent calculation basis is given by the bonding and anti-bonding states $|b\rangle$ and $|a\rangle$:

$$|\psi\rangle = \alpha|b\rangle + \beta|a\rangle, \tag{13}$$

As shown in Sec. 4.2, the energy gap between the anti-bonding and bonding states here is given by $\sqrt{(\delta E)^2 + 4t^2}$.

In the first scheme where $|l\rangle$ and $|r\rangle$ are the calculation basis states, the charge distribution between the two dots and thereby the polarization of the double dot directly reflects the classical part of the qubit information content. Such a spatial resolution is desirable for fast readout of the qubit value by coupling a charge detector to the double quantum dot, e.g., a quantum point contact, an additional quantum dot or a single electron transistor.

The time available for any quantum mechanical computation is ultimately limited by the coherence time (τ_{coh}) of the electronic states in the double quantum dot. The coherent charge oscillation has a Rabi frequency of $\Omega_0 = 2t/h$, giving a lower limit for the time required by a single operation.

Spin-based qubits. − As proposed by Loss and DiVincenzo [11], the spin states of a single excess electron in a quantum dot form a natural calculation basis for a qubit:

$$\left|\uparrow_z\right\rangle \equiv |0\rangle, \qquad \left|\downarrow_z\right\rangle \equiv |1\rangle . \tag{14}$$

The double quantum dot here comprises the next step of integration, namely the direct coherent and controllable coupling of two qubits via the Heisenberg exchange interaction. With this respect it has recently been the object of detailed theoretical research [11, 56] – for all quantum computing schemes, such a coupling of qubits by two-qubit gates is an important prerequisite. Furthermore, the electronic spin states have been shown to possess a much longer decoherence time compared to the charge degree of freedom [57, 58]; decoherence is mainly introduced by the spin-orbit and hyperfine [59] interaction.

7 Conclusion

We have seen that coupled quantum dots can be readily manufactured in a variety of geometries. For studying single electron tunneling and coherent modes in the coupled dots we have chosen a serial geometry. This allowed us to perform transport measurements ranging from direct-current into the microwave regime. We were able to demonstrate tuning of the coherent coupling for direct as well as for photon assisted transport. In an advanced setup two dots were coupled in parallel. With this configuration we probed Aharonov-Bohm oscillations demonstrating phase coherence. To form realistic single or coupled qubits, dephasing as a major problem need to be solved. Engineering of quantum dot structures and its host materials would provide the knowledge of dephasing mechanisms in solid-state quantum dot system [60]. Dynamic control and read-out of single and coupled qubits will finally enable us to construct more complex and functional quantum circuits.

References

[1] M. A. Kastner, Phys. Today **46**(1), 24 (1993).
[2] D. Heitmann and J. P. Kotthaus, Phys. Today **46**(6), (1993).
[3] L. P. Kouwenhoven, Science **268**, 1440 (1995).
[4] R. C. Ashoori, Nature (London) **379**, 413 (1996).
[5] R. H. Blick, R. J. Haug, J. Weis, D. Pfannkuche, K. von Klitzing, and K. Eberl, Phys. Rev. B **53**, 7899 (1996).

[6] L. P. Kouwenhoven, C. M. Marcus, P. L. McEuen, S. Tarucha, R. M. Westervelt, and N. S. Wingreen, in: Mesoscopic Electron Transport, edited by L. L. Sohn, L. P. Kouwenhoven, and G. Schön (Kluwer, Dordrecht, 1997), Series E, Vol. 345, pp. 105–204.

[7] H. Grabert and M. H. Devoret, eds., Single Charge Tunneling (Plenum, New York, 1992), Ser. B, Vol. 294.

[8] A. Barenco, D. Deutsch, A. Ekert, and R. Jozsa, Phys. Rev. Lett. **74**, 4083 (1995).

[9] R. Landauer, Science **272**, 1914 (1996).

[10] A. O. Orlov, I. Amlani, G. H. Bernstein, C. S. Lent, and G. L. Snider, Science **277**, 928 (1997).

[11] D. Loss and D. P. DiVincenzo, Phys. Rev. A **57**, 120 (1998).

[12] A. Kumar, Surf. Sci. **263**, 335 (1992).

[13] M. Stopa, Phys. Rev. B **54**, 13767 (1996).

[14] C. W. J. Beenakker, Phys. Rev. B **44**, 1646 (1991).

[15] M. Kemerink and L. W. Molenkamp, Appl. Phys. Lett. **65**, 1012 (1994).

[16] F. R. Waugh, M. J. Berry, D. J. Mar, R. M. Westervelt, K. L. Campman, and A. C. Gossard, Phys. Rev. Lett. **75**, 705 (1995).

[17] C. Livermore, C. H. Crouch, R. M. Westervelk, K. L. Campman, and A. C. Gossard, Science **274**, 1332 (1996).

[18] R. H. Blick, D. Pfannkuche, R. J. Haug, K. v. Klitzing, and K. Eberl, Phys. Rev. Lett. **80**, 4032 (1998).

[19] W. G. van der Wiel, S. De Franceschi, J. M. Elzerman, T. Fujisawa, S. Tarucha, and L. P. Kouwenhoven, Rev. Mod. Phys. **75**, 1 (2003).

[20] For simplicity, here we drop the contribution from the discrete electronic states: $\epsilon_N - \epsilon_{N-1}$.

[21] C. A. Stafford and Ned S. Wingreen, Phys. Rev. Lett. **76**, 1916 (1996).

[22] T. H. Stoof and Yu. V. Nazarov, Phys. Rev. B **53**, 1050 (1996).

[23] D. M. Cardamone, C. A. Stafford, and B. R. Barrett, phys. stat. sol. (b) **230**, 419 (2002).

[24] R. H. Blick, R. J. Haug, D. W. van der Weide, K. von Klitzing, and K. Eberl, Appl. Phys. Lett. **67**, 3924 (1995).

[25] T. H. Oosterkamp, L. P. Kouwenhoven, A. E. A. Koolen, N. C. van der Vaart, and C. J. P. M. Harmans, Phys. Rev. Lett. **78**, 1536 (1997).

[26] H. Qin, F. Simmel, R. H. Blick, J. P. Kotthaus, W. Wegscheider, and M. Bichler, Phys. Rev. B **63**, 035320 (2001).

[27] H. Qin , D. W. van der Weide, J. Truitt, K. Eberl, and R. H. Blick, Nanotechnology **14**, 60 (2003).

[28] R. H. Blick, R. J. Haug, K. von Klitzing, and K. Eberl, Surf. Sci. **361–362**, 595 (1996).

[29] T. Fujisawa and S. Tarucha, Superlattices Microstruct. **21**, 247 (1997).

[30] T. H. Oosterkamp, T. Fujisawa, W. G. van der Wiel, K. Ishibashi, R. V. Hijman, S. Tarucha, and L. P. Kouwenhoven, Nature (London) **395**, 873 (1998).

[31] A. W. Holleitner, H. Qin, F. Simmel, B. Irmer, R. H. Blick, J. P. Kotthaus, A. V. Ustinov, and K. Eberl, New J. Phys. **2**, 3.1–3.7 (2000).

[32] H. Qin, A. W. Holleitner, K. Eberl, and R. H. Blick, Phys. Rev. **64**, 241302(R) (2001).

[33] T. Fujisawa, W. G. van der Wiel, and L. P. Kouwenhoven, Physica E **7**, 413 (2000).

[34] D. V. Averin and Yu V. Nazarov, in: Single Charge Tunneling, edited by H. Grabert and M. H. Devoret (Plenum, New York, 1992), Ser. B, Vol. 294, pp. 217–247.

[35] M. A. Nielsen and I. L. Chuang, in: Quantum Computation and Quantum Information (Cambridge Univ. Press, Cambridge, 2000).

[36] D. Loss and E. V. Sukhorukov, Phys. Rev. Lett. **84**, 1035 (2000).

[37] A. W. Holleitner, C. R. Decker, H. Qin, K. Eberl, and R. H. Blick, Phys. Rev. Lett. **87**, 256802 (2001).

[38] A. W. Holleitner, R. H. Blick, A. K. Hüttel, K. Eberl, and J. P. Kotthaus, Science **297**, 70 (2002).

[39] A. W. Holleitner, R. H. Blick, and K. Eberl, Appl. Phys. Lett. **82**, 1887 (2003).

[40] A. W. Holleitner, H. Qin, R. H. Blick, K. Eberl, and J. P. Kotthaus, Physica E **12**, 774 (2002).

[41] L. Onsager, Nuovo Cimento, Suppl. 2 **6**, 249 (1949).

[42] A. L. Yeyati and M. Büttiker, Phys. Rev. B **52**, R14360 (1995).

[43] A. Yacoby, M. Heiblum, D. Mahalu, and Hada Shtrikman, Phys. Rev. Lett. **74**, 4047 (1995).

[44] E. Buks, R. Schuster, M. Heiblum, D. Mahalu, and V. Umansky, Nature (London) **391**, 871 (1998).

[45] A. W. Holleitner, A. Chudnowski, D. Pfannkuche, K. Eberl, and R. H. Blick, subm. to Phys. Rev. B.

[46] J. Kondo, Prog. Theor. Phys. **32**, 37 (1964).

[47] D. Goldhaber-Gordon, H. Shtrikman, D. Mahalu, D. Abusch-Magder, and U. Meirav, Nature **391**, 156 (1998).

[48] S. M. Cronenwett, T. H. Oosterkamp, and L. P. Kouwenhoven, Science **281**, 540 (1998).

[49] J. Schmid, J. Weis, K. Eberl, and K. v. Klitzing, Physica B (Amsterdam) **256**, 182 (1998).

[50] F. Simmel, R. H. Blick, J. P. Kotthaus, W. Wegscheider, and M. Bichler, Phys. Rev. Lett. **83**, 804 (1999).

[51] J. Schmid, J. Weis, K. Eberl, and K. v. Klitzing, Phys. Rev. Lett. **84**, 5824 (2000).

[52] G. Zarand, Phys. Rev. B **52**, 13459 (1995).

[53] G. Zarand and K. Vladar, Phys. Rev. Lett. **76**, 2133 (1996).

[54] L. Borda, G. Zarand, W. Hofstetter, B. I. Halperin, and J. v. Delf, Phys. Rev. Lett. **90**, 026602 (2003).

[55] D. Boese, W. Hofstetter, and H. Schoeller, Phys. Rev. B **66**, 125315 (2002).

[56] X. Hu and S. Das Sarma, Phys. Rev. A **61**, 062301 (2000).

[57] T. Fujisawa, D. G. Austing, Y. Tokura, Y. Hirayama, and S. Tarucha, Nature **419**, 278 (2002).

[58] A. K. Hüttel, H. Qin, A. W. Holleitner, R. H. Blick, K. Neumaier, D. Weinmann, K. Eberl, and J. P. Kotthaus, Europhys. Lett. **62**, 712 (2003).

[59] A. K. Hüttel, J. Weber, A. W. Holleitner, D. Weinmann, K. Eberl, and R. H. Blick, Phys. Rev. B **69**, 073302 (2004).

[60] R. H. Blick, A. K. Hüttel, A. W. Holleitner, E. M. Höhberger, H. Qin, J. Kirschbaum, J. Weber, W. Wegscheider, M. Bichler, K. Eberl, and J. P. Kotthaus, Physica E **16**, 76 (2003).